Atomic Layer Deposition for Tuning the Surface Chemical Composition of Nickel Iron Phosphates for Oxygen Evolution Reaction in Alkaline Electrolyzers

Ruben Blomme*[1], Rahul Ramesh*[1], Lowie Henderick[1], Matthias Minjauw[1], Philippe Vereecken[2,3,4], Mieke Adriaens[5], Christophe Detavernier[1], and Jolien Dendooven[1]

[1]Ghent University, Department of Solid State Sciences, Conformal Coating of Nanostructures (CoCooN), Krijgslaan 281 S1, 9000 Ghent (Belgium)
[2]imec, Kapeldreef 75,3001 Leuven (Belgium)
[3]KU Leuven, Department of Microbial and Micromolecular systems (M2S), cMACS, Celestijnenlaan 200F, 3001 Leuven (Belgium)
[4]Energyville, Thor Park 8320, 3600 Genk (Belgium)
[5]Ghent University, Department of Chemistry, Faculty of Sciences, 9000 Ghent (Belgium)

January 23, 2024

Abstract

Abstract

Transition metal phosphates are promising catalysts for the oxygen evolution reaction (OER) in alkaline medium. Herein, Fe-doped Ni phosphates are deposited using plasma-enhanced atomic layer deposition (PE-ALD) at 300°C. A sequence of f Fe phosphate PE-ALD cycles and n Ni phosphate PE-ALD cycles is repeated x times. The Fe to Ni ratio can be controlled by the cycle ratio (f/n), while the film thickness can be controlled by the number of cycles (x times (n+f)). 30 nm films with an Fe/Ni ratio of ∼10% and ∼37%, respectively, are evaluated in 1.0 M KOH solution. Remarkably, a significant difference in OER activity is found when the order of the Ni and Fe phosphate PE-ALD cycles in the deposition sequence is reversed. A 20 to 45% larger current density is obtained for catalysts grown with an Fe phosphate PE-ALD cycle at the end compared to the Ni phosphate-terminated flavour. We attribute this to a higher concentration of Fe centers on the surface, as a consequence of the specific PE-ALD approach. Secondly, increasing the thickness of the catalyst films up to 160 nm results in an increase of the OER current density and active surface area, suggesting that the as-deposited smooth and continuous films are converted into electrolyte-permeable structures during catalyst activation and operation. This work demonstrates the ability of PE-ALD to control both the surface and bulk composition of thin film electrocatalysts, offering valuable opportunities to understand their impact on performance.

Keywords— ALD, Atomic Layer Deposition, OER, Oxygen Evolution Reaction, Electrocatalysis, Water Splitting, Nickel, Iron, Phosphates, Thin Films

Introduction

One of the main methods of achieving carbon neutrality by 2050 is by using more H_2 [1]. Due to its CO_2 free combustion, H_2 is able to decarbonise many essential sectors such as long haul transport and steel production [2]. However the current main industrial production method of H_2 requires fossil fuels and has to be replaced by alternative green H_2 production methods based on water electrolysis. This will require a tremendous increase in dedicated renewable energy infrastructure. H_2 can also be used in the electric power sector to capture excess energy in periods of high production from renewables due to its high energy density.

Electrochemical water splitting consists of two reactions, namely the cathodic Hydrogen Evolution Reaction (HER) and the anodic Oxygen Evolution Reaction (OER). Both of these reactions have an associated overpotential, the latter however has the highest. This is due to the complexity of the OER mechanism involving the transfer of four electrons ($4\ OH^- \leftrightarrow 2\ H_2O + O_2 + 4\ e^-$, in alkaline medium). Kinetically, the OER can proceed via a multi-step process with a coupled transfer of one proton and one electron at each step [3] [4]. The high energy barriers involved make the OER kinetics slow and result in a substantial overpotential.

This overpotential, next to membrane resistance and system architecture, is one of the primary detriments for an efficient production of hydrogen and is thus the most important obstacle that should be tackled before the widespread production of green H_2 on a large scale is broadly implemented. Addressing this challenge necessitates the advancement of electrolyzer systems which could be done by developing exceptional electrocatalyst to boost performance[5].

In an attempt to tackle this production inefficiency, transition metal-based catalysts in alkaline conditions have already been proposed in literature as low-cost, earth-abundant and highly active alternatives to the traditional noble metal catalysts for the OER in acidic conditions [6]. A wide range of transition metal combinations, created with various synthesis methods, have already been investigated [7]. Among the most promising materials within this selection are mixed nickel-iron based catalysts of the layered hydroxide and spinel types. Trotochaud et al. thoroughly investigated the effect of Fe-incorporation in Ni hydroxides and showed that the OER performance of $Ni(OH)_2$ increased significantly for an Fe/(Fe+Ni) ratio as low as 5% [8]. Landon et al. and Trotochaud et al. both concluded that their best performing mixed metal oxide catalysts contained 10% Fe and 90% Ni [9][10], while Louie et al. stated that the 40% Fe sample proved to be the best performing candidate of a wide range of Fe:Ni combinations, showing a slight improvement over a 15% Fe sample [11].

In addition to oxides and hydroxides, more recent work has explored the performance of phosphate materials, inspiring also the present study. Crystalline as well as amorphous phosphates with promising OER activity have been synthesized [12] [13] [14] [15]. Also phosphonate materials have shown promising results for the deposition of OER-catalysts [16]. The overpotential and Tafel slopes were reported to be lower for Ni-based phosphates than for other Ni-based OER catalysts, as summarized by Guo et al. in 2018 [17]. Multi-metallic compounds often show improved performance [12]. A recent publication by Lin et al. examined a Ni-Fe phosphate material on graphite, confirming the best performance for a 15% Fe mixed phosphate [18].

The superior OER activity has been attributed to different roles of the phosphate groups. On the one hand, phosphate groups are proposed to assist the OER by acting as adsorption site for water molecules and as proton acceptor facilitating charge transfer [17]. The amount of phosphate sites, the type of phosphate anion and the structural network have been suggested to impact the adsorption capacity and proton-conducting pathways [13] [14]. On the other hand, phosphates are supposed to be pre-catalysts: under the oxidizing OER potentials the phosphate surface groups impact the surface reconstruction of the catalyst yielding more active catalytic centers, often of the oxyhydroxide type [19]. Li et al. showed that the surface of a Co oxide catalysts functionalized with phosphate ions transforms into more active CoOOH surface species than a native Co oxide surface [20]. However, the relationship between the precatalyst surface and activity is still ambiguous, especially for amorphous materials. Accordingly, exerting control over the surface species and composition offers options to enhance and study their impact on the overall performance of the material.

In this work, atomic layer deposition (ALD) was employed to deposit iron-doped nickel phosphate

OER catalysts with excellent control over the internal composition as well as the composition of the surface-terminating layer. ALD is a thin film deposition method known for its superior uniformity and conformality on complex 3D substrates. A wide variety of ALD process chemistries is available that yield phosphate materials with different phosphorous content, ranging from P-rich to P-doped materials [21][22]. ALD-grown phosphates have found applications in Li-ion battery electrode design [21], while a few works have studied amorphous cobalt phosphates for OER catalysis [6] [15] [22][23]. To the best of our knowledge, there has been no exploration of bimetallic phosphate materials deposited via ALD for the Oxygen Evolution Reaction. As this field evolves and garners more attention, the prospect of creating intricate materials aligning with contemporary non-noble metal catalysts should be a valuable addition to the catalogue of ALD-deposited electrochemical catalyst materials.

Methods

ALD-system

The plasma enhanced atomic layer deposition (PE-ALD) system used to perform all of the depositions is a custom-built high vacuum pump type system. A backing pump evacuates the chamber to a low vacuum around 10^{-2} mbar after which a turbomolecular pump evacuates the chamber to a high vacuum ranging from 1 - 5 $\times$ 10^{-6} mbar. The flow of the precursor vapors into the reactor chamber was regulated through computer controlled pneumatic valves and their partial pressures were regulated by manually adjustable needle valves.

The precursors used for this deposition were trimethylphosphate used as a plasma at 200W (TMP*, Sigma Aldrich, 97%, CAS: 512-56-1), t-butylferrocene (TBF, Strem Chemicals Inc., 98%, CAS: 1316-98-9) and bicyclopentadienylnickel ($NiCp_2$, Sigma Aldrich, 99%, CAS: 1271-28-9). Additionally O_2 was used as a plasma at 300W (O_2*). The plasma was generated inside of a fuzed quartz column with a copper coil wrapped around. This coil was connected to a 13.56 MHz RF generator (ENI GHW-12Z) capable of changing the delivered power after each step of the ALD process. The temperature of the precursor bottles was respectively 40-45°C, 85°C and 80°C. The precursor delivery lines, connecting precursor bottles to the deposition chamber, were heated to 55°C, 95°C and 90°C respectively to prevent condensation. The walls of the deposition chamber were heated to 120°C. An overview of the process conditions is given in the results section.

Material Characterisation

During the depositions in-situ ellipsometry was performed using a Filmsense Ellipsometer. Fitting of the ellipsometry data was done using a three layer model consisting of a Cauchy layer, native oxide layer and a heated silicon substrate layer. The thickness of the native oxide varied between samples but never exceeded 5 nm. To verify the optical model, an X-ray reflectivity (XRR) measurement (Bruker, Model D8) using Cu-Kα radiation was always performed on the deposited film and the final film thicknesses were compared and found to be in good agreement. X-ray fluorescense measurements were conducted using a Bruker ArtaX spectrometer with a silicon-based energy dispersive X-ray detector (XFlash).

X-ray photoelectron spectroscopy (XPS) was performed using a Thermo Scientific Theta Probe XPS-instrument using Al Kα rays generated at 15 kV and 70 W and focused to a spot size of 0.3 mm by an MXR1 monochromator. For depth profiling, the surface of the samples was etched by Ar^+ ions at an accelerating voltage of 3 keV and a current of 2 µA into an area of 2 mm x 2 mm. Calibration of all the spectra was performed using the adventitious C 1s-peak present on the sample surface; the energy attributed to this peak was 284,6 eV.

To conduct atomic force microscopy (AFM) a Dimension Edge system (Bruker) using Tespa-V2 tips (nominal tip size of 7 nm, maximal tip size of 10 nm) was used in tapping mode.

Electrochemical Characterisation

Electrochemical characterizations were performed in a three-electrode cell using a rotating disc electrode (RDE) setup connected to a potentiostat/galvanostat (Metrohm Autolab PGSTAT30, analysis and processing with Nova software). Potentials were obtained using a HgO/Hg reference electrode and were converted to reversible hydrogen electrode potentials using the following equation:

$$U_{RHE} = U_{HgO/Hg} + U^0_{HgO/Hg} + 0.0592V \times pH$$

Where $U_{HgO/Hg}$ is an applied potential, pH = electrolyte pH and $U^0_{HgO/Hg}$ is the standard potential of the HgO/Hg electrode in 1 M NaOH (0.120 V [24]). The working electrode was created by depositing the ALD-material of interest onto a conducting substrate. The chosen substrate was a Ni-disc, cut from a Ni-rod with a diameter of .6 cm, which was mirror polished and finished with a 150 nm Ni film, deposited by dc magnetron sputtering method. Figure S1 in Supporting Material shows the schematic of a mounted sample on the RDE. The exposed area of the electrode was 0.28 cm^2.

The used reference electrode is a mercuric oxide-mercury electrode (HgO/Hg in 1 M NaOH, RE-61AP reference electrode from ALS Co. Ltd), the counter electrode a platinum wire (Biologic). The electrolyte used for the study is 1M KOH (semiconductor grade 99.99% trace metals basis). The experiments were conducted at a rotation speed of 900 rpm.

The measuring procedure consists of three steps, an overview of which is given in Figure 1. First, chronopotentiometry (CP) is performed at 50 mA/cm^2, 25 mA/cm^2, 10 mA/cm^2, 2 mA/cm^2 and finally 50 mA/cm^2. Each value is held for 30 minutes. After this initial step a decrease in required overpotential is generally observed indicating that the material has activated slightly.

Secondly, after the initial CP, electrochemical impedance spectroscopy (EIS) from 100 kHz to 1 Hz at 100 mV RMS is performed to determine the uncompensated resistance, used to apply iR compensation (uncompensated resistance was determined at 100 kHz). The third and final measurement is a cyclic voltammetry (CV) measurement which sweeps 10 times from 0.2 V to 0.7 V (vs. HgO/Hg electrode) at a scan rate of 1 mV/s. This measurement is 85% iR-corrected to minimize possible influences due to the ohmic drop. An overview of good practices for iR-correction is given in the work by Anantharaj et al.[25].

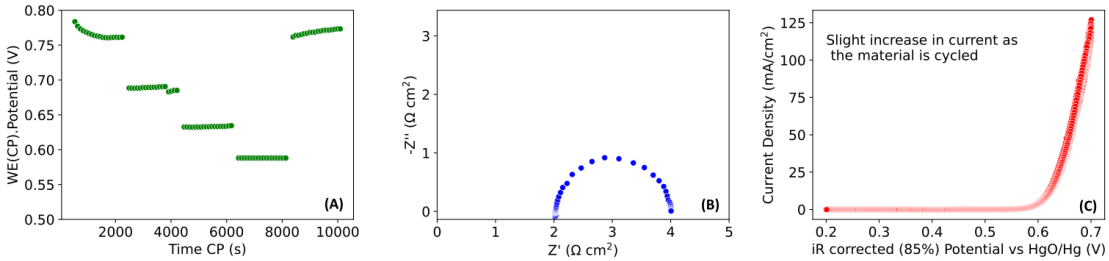

Figure 1: Overview of the experiments performed on the as-deposited materials. (A) CP measurements at 50, 25, 10, 2 and again 50 mA/cm^2. On the given graph a shift in potential due to the decrease in surface area caused by the formation of a gas bubble is visible. (B) EIS measurement taken at 0.626 V vs. HgO/Hg.(C) 10 CV cycles; over the course of the experiment the current increases slightly as can be seen in this exemplary dataset.

Results and Discussion

Atomic Layer Deposition of Ni- and Fe-phosphates and Mixed Materials

This work is based on the ALD processes for nickel and iron phosphate materials, which will be henceforth addressed as NiPO and FePO, respectively. The used processes were both previously reported by our group. The FePO process was reported by Dobbelaere et al. [26] in 2016 and the NiPO process was described by Henderick et al. [27] in 2022. Both of the ALD-sequences are constructed similarly: a TMP plasma (TMP*) pulse is followed by a O_2* pulse and finally the metalorganic precursor ($NiCp_2$ or TBF) is pulsed with argon carrier gas. An overview of the experimental parameters is presented in Table 1.

The choice of TMP* over a regular, thermal TMP precursor pulse was made because of its higher reactivity and its tendency to introduce more phosphorous into the deposited film. TMP* processes exhibit a higher growth per cycle (GPC) than their thermal equivalents. This can be understood based on the proposed mechanism [28]: the TMP* undergoes a polymerizing reaction in the plasma which results in the deposition of an organophosphate layer onto the material, which is transformed into a phosphoric acid-like layer by the exposure to O_2*. The polymerization reaction is very temperature-dependent: an uncontrolled, continuous growth takes place at temperatures below 225 °C, while self-terminating growth occurs at 300 °C. Therefore, the substrate temperature is set at 300 °C for all depositions in this work.

By combining the NiPO and FePO ALD cycles in a supercycle, a new bimetallic phosphate material is deposited in this work. A schematic of the approach is given in Figure 2. Tuning the fraction of FePO (f) relative to NiPO (n) ALD cycles determines the composition of the amorphous NiFePO materials. The cycle ratio (CR) is defined for FePO as $CR_{Fe} = f/(f+n)$ and NiPO as $CR_{Ni} = 1 - CR_{Fe} = n/(f+n)$. In this work, the processes for the NiFePO materials are labeled as NiPO-FePO (n-f). The bold font indicates the material that is deposited last in the ALD supercycle (see Figure 2). It should be noted that all samples in this section regarding the ALD properties were deposited using a **NiPO**-FePO type supercycle approach.

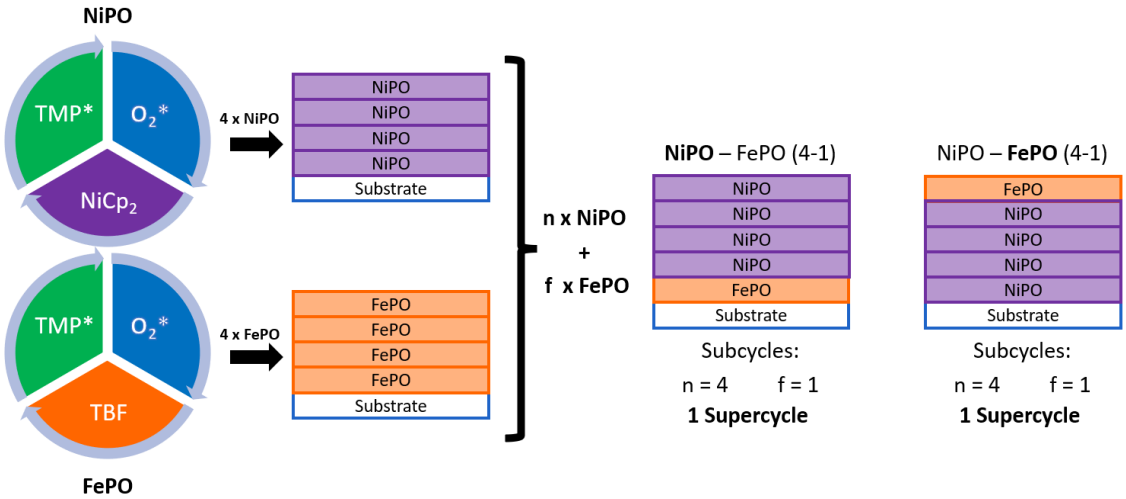

Figure 2: Schematic overview of the combination of the individual NiPO and FePO ALD processes into a supercycle to deposit bimetallic Ni-Fe phosphates. By varying the fraction of FePO relative to NiPO ALD cycles, f/n, amorphous NiFePO materials with different composition are deposited. The cycle ratio (CR) is defined for FePO as $CR_{Fe} = f/(f+n)$ and NiPO as $CR_{Ni} = n/(f+n)$. The processes for the NiFePO materials are labeled as NiPO-FePO (n-f). The bold font in p.e. **NiPO**-FePO indicates that NiPO was deposited last in the ALD supercycle.

The deposition conditions for the NiPO process were identical to the original work [27]; the FePO process, however, was adapted to better suit the selected application of OER catalysis. As highlighted in the introduction, the highest OER activity is usually obtained when Fe is present as a dopant in Ni-based catalysts. When a supercycle approach is used in ALD, a lower GPC offers a finer control over the dopant concentration. However, an exceptionally high GPC of 1.1 nm per

cycle was reported for the FePO process [26], compared to a value of 0.2 nm per cycle for the NiPO process [27]. No significant increase in the film thickness occurred when pulsing times in excess of the given exposure times (Table 1) were used, suggesting that the saturation which was present for the indiviual processes still holds.
To lower the GPC of the FePO process in the ALD supercycle to ca. 0.2 nm per cycle, a dynamic pulsing approach was chosen over the previously used static pulsing approach. In the dynamic mode, the TBF precursor (with Ar) is introduced while the chamber is continuously pumped by a turbomolecular pump, while in the static mode the valve to the pump is closed thus creating a higher pressure inside the reactor chamber. A comparison of the FePO GPC against exposure time for the two pulsing modes is given in Figure S2 in Supporting Materials. In both cases, a quasi-saturation behaviour is observed: the increase in GPC with exposure time clearly slows down after 30 s exposure.

Parameter	TMP-plasma*	O_2-plasma*	$NiCp_2$+Ar	TBF+Ar
Pressure (mbar)	8.0×10^{-4}	1×10^{-2}	6.5×10^{-3}	6.5×10^{-3}
Exposure time (s)	10	10	20	30
Pumping time (s)	140	40	60	60
Precursor heating (°C)	45	RT	80	80

Table 1: Table summarizing the ALD process conditions. The TMP* vapour pressure is kept low to minimize condensation on the walls of the plasma column. The "sticky" properties of this vapour drastically increase the duration of the pumping steps in between the different precursor exposures. Both $NiCp_2$ and TBF require argon as carrier gas. RT indicates that the precursor was delivered at room temperature (approx. 20 °C).

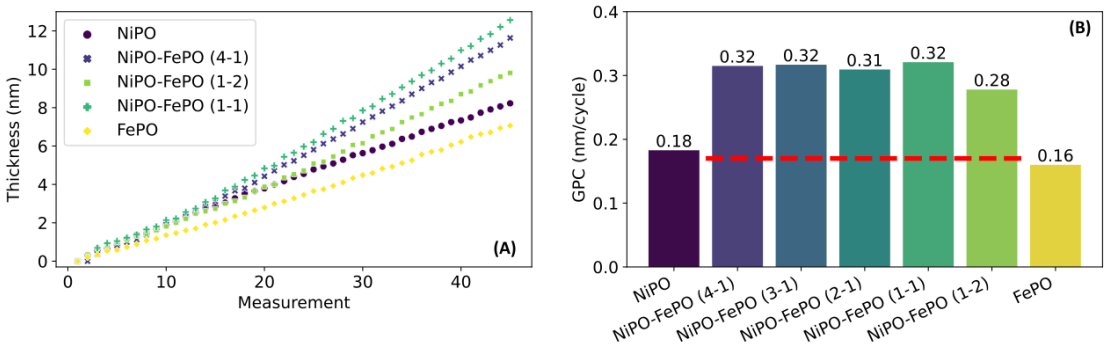

Figure 3: (A) Ellipsometry data for the growth of PE-ALD-deposited materials with varying composition on Si substrate. Measurements were taken after the metalorganic precursor step of each NiPO and FePO ALD cycle in the supercycle. (B) Overview of the average GPC for processes with different FePO and NiPO ALD cycle sequences in the supercycle. A clear difference between the pure processes and the mixed processes is observed. The red dashed line indicates the expected GPC.

Various Fe-doping levels in NiPO could now be obtained by changing the fraction of FePO ALD cycles relative to NiPO ALD cycles in the supercycle, f/n. Graph A of Figure 3 depicts the in-situ ellipsometry data for the growth of selected NiFePO materials. The thickness was measured after each metalorganic precursor step, i.e. after each NiPO or FePO ALD cycle in the supercycle. All curves in the graph show a similar behaviour for the initial 10-15 ALD cycles before they diverge. This substrate enhanced initial growth was previously already observed in the depostion of undoped NiPO materials and is thus attributed to the NiPO contribution in the supercycle[27]. The slopes of the growth curves clearly differ between the pure materials and the combined materials. As no obvious differences in the thickness addition per individual NiPO and FePO ALD cycle in a supercycle could be observed, the slope of the growth curves is interpreted as an average GPC for both NiPO and FePO ALD cycles. It is found that pure NiPO grows at 0.18 nm/cycle and pure FePO at 0.16 nm/cycle, while the combined materials grow at ca. 0.30 nm/cycle.

Expected growth behaviour for a combined ALD process employing a supercycle would be the addition of the individual processes, referred to as the rule of mixtures [29]. Thus, the expected average GPC for a 1 NiPO - 1 FePO process would be (0.18 nm/cycle + 0.16 nm/cycle)/2 = 0.17 nm/cycle and not the observed 0.32 nm/cycle. The bar graph in Figure 3 B synopsizes the observed average GPC values, while the red dashed line indicates the expected GPC based on the rule of mixtures.

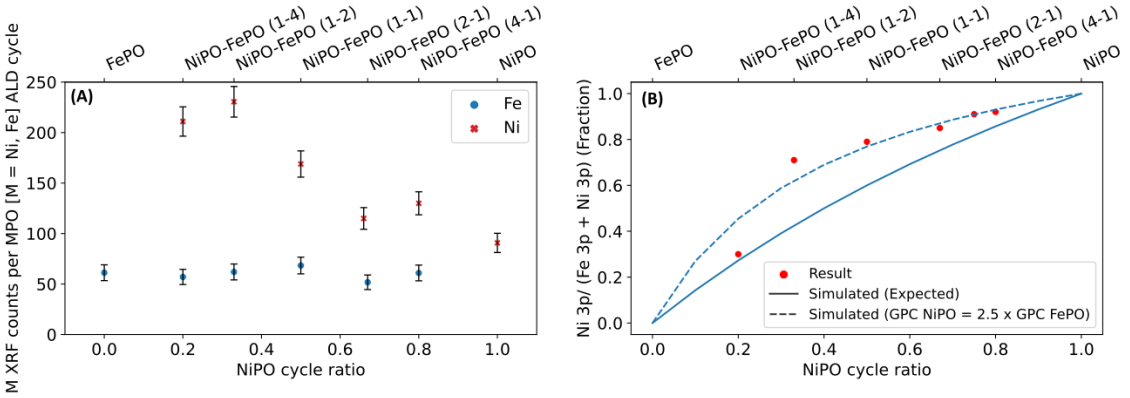

Figure 4: (A) Graph depicting the Ni and Fe XRF-counts divided by the total number of NiPO and FePO cycles, respectively. The normalized Ni-counts increase for decreasing NiPO cycle ratio, while the normalized Fe-counts remain mostly around the same value. (B) Graph showing the Ni-fraction of the metal present. Two models were plotted Data obtained from XPS. Results are compared to expected composition and a simulation.

To study this unexpected discrepancy in GPC, XRF and XPS measurements were performed to compare the compositions of the different materials and link them to their GPCs. The results of the XRF measurements of samples with varying NiPO cycle ratios ($CR_{Ni} = n/(f+n)$) are displayed in graph A of Figure 4. The data points correspond to the measured Ni and Fe XRF counts divided by the number of applied NiPO and FePO ALD cycles, respectively. Thus, to construct the graph the total Ni [Fe] counts are divided by the number of ALD supercycles and then divided by the number of NiPO [FePO] ALD cycles in that supercycle (e.g. 2000 Ni counts for 10 supercycles with $n = 2$ and $f = 1$ would be 100 counts/10/2 = 100 Ni counts in the graph). This presentation of the data provides an insight in the relative efficiency at which Ni and Fe are incorporated in the layer for different NiPO cycle ratios. Iron is steadily incorporated independently of the NiPO cycle ratio. Nickel however seems to get incorporated more efficiently as the overall NiPO cycle ratio decreases. The normalized Ni XRF contribution increases from 100 counts for a pure NiPO process to more than 200 counts for a NiPO-FePO (1-4) process ($CR_{Ni} = 0.2$).

Results from XPS measurements corroborated these findings. Plot B in Figure 4 shows the nickel metal fraction against the NiPO cycle ratio in the ALD sequence. To construct the graph, the normalized peak area of the Ni 3p XPS signal is divided by the summed areas of the Fe 3p and Ni 3p peaks. Herein, the normalized peak area is obtained by dividing the background-subtracted peak area by the relative sensitivity factor. Representative XPS spectra and backgrounds are shown in Figure S3 in Supporting Materials. Note that Fe 3p and Ni 3p peaks are analysed instead of the traditional Fe 2p and Ni 2p peaks to prevent Ni Auger peaks influencing the Fe 2p signal and vice versa [30].

To interpret the XPS results shown in Figure 4 (B), the modelling of the composition of a ternary oxide based on the rule of mixtures served as inspiration [29]. Here we assume NiPO and FePO to be the two components of the film, such that the expected composition of a bimetallic oxide/phosphate can be obtained from the following equations:

$$\text{Composition (fraction of NiPO)} = \frac{\rho_{Ni} \cdot GPC_{Ni} \cdot CR_{Ni}}{\rho_{Ni} \cdot GPC_{Ni} \cdot CR_{Ni} + \rho_{Fe} \cdot GPC_{Fe} \cdot CR_{Fe}}$$

with $GPC_{Ni} = 0.18$ nm/cycle, $GPC_{Fe} = 0.16$ nm/cycle, $\rho_{Ni} = 4\ g/cm^3$, $\rho_{Fe} = 3\ g/cm^3$ and $CR_{Fe} = 1 - CR_{Ni}$.

The density values were approximated from XRR measurements of the pure NiPO and FePO materials (Figure S4 in Supporting Materials), and can be compared with values reported for crystalline $Ni_3(PO_4)_2$ = 4.38 g/cm^3, $FePO_4$ = 3.06-2.87 g/cm^3 and $Fe_3(PO_4)_2$ = 2.61 g/cm^3 for reference. When we simulate a simple curve using these values it does not match the observed fractions (see Figure 4 (B)). The measured Ni content in the mixed materials is systematically higher than the expected content assuming the GPCs for the pure NiPO and FePO ALD processes. This is in line with the conclusion from the XRF measurements.

To get to a better agreement between the calculations and the experimental values, the ratio of the NiPO to FePO GPC had to be artificially increased to 2.5, again suggesting a more efficient incorporation of Ni per ALD cycle in a mixed ALD process than in a pure NiPO deposition. However, despite this seemingly erratic growth, the Ni (and thus also Fe) content can still be tuned via the cycle ratio, especially if low Fe concentrations are targetted, as is the case here for the application of OER electrocatalysis.

The reason for the enhanced Ni incorporation with decreasing NiPO cycle ratio is still unclear, even if some hypotheses can be discarded based on additional experiments we did. Differences in surface roughness for varying NiPO cycle ratios can be excluded. NiPO - FePO (4-1) and NiPO - FePO (1-4), the two films with the most diverging cycle ratios, were studied with AFM but neither showed significant roughness or difference in roughness with RMS values of 0.33 nm and 0.26 nm, respectively. Secondly, decomposition of the precursors was also investigated on all relevant surfaces. TBF nor $NiCp_2$ showed signs of decomposition on SiO_2, FePO or NiPO surfaces as was confirmed by in-situ ellipsometry experiments (Figure S5 in Supporting Materials). We reason that the presence of the FePO creates reactive species favorable for the NiPO to be incorporated into the film, but investigating the nature of these requires additional in-situ characterizations of the nucleation effects during ternary phosphate ALD. Literature reports on ALD of ternary oxides involving NiO and/or Fe_2O_3 ALD with cyclopentadienyl-based precursors could serve as a starting point for this. Indeed, in several cases deviation from the rule of mixture has been reported. In the case of NiFeO ALD, Ni-rich materials are typically obtained,[31, 32] similar to the observations in this work. Chong et al. linked the higher uptake of Ni relative to Fe to the higher reactivity of nickelocene with respect to ferrocene [31]. More recent studies reported an enhanced growth per cycle for Al_2O_3 ALD when combined with NiO ALD or Fe_2O_3 ALD in a supercycle to deposit NiAlO or FeAlO ternary materials, respectively [33, 34]. The authors related this observation to the presence of reactive oxygen species in NiO or Fe_2O_3 films deposited with ozone as co-reactant [34, 35].

Film Characteristics

The XPS-data compiled in Table 2 present an overview of the composition of the mixed materials deposited in this work. The atomic concentrations are obtained by quantifying the C 1s, Fe 3p, Ni 3p, O 1s and P 2p regions after background subtraction. Representative XPS spectra and backgrounds are shown in Figure S3 in Supporting Materials, together with a survey spectrum (Figure S6). No C is present in the films. As the NiPO cycle ratio increases the atomic concentration of Ni increases drastically from the (1-4) sample to the (1-2) sample and then steadily increases further. Notably, Fe decreases in the same manner. Both P and O remain quite stable for the different processes, as does the overall metallic fraction which remains at 13-14%. The metal to phosphorous ratio of the material remains stable throughout the different deposition combinations with both the NiPO-FePO 4-1 and 1-4 having slightly more metal. Based on the M/P and the

Sample	CR_{Ni}	C (at%)	Fe (at%)	Ni (at%)	O (at%)	P (at%)	M/P	P/O
FePO	0.0	0.0	13.7	0.0	61.3	25.1	0.55	0.41
NiPO-FePO (1-4)	0.2	0.0	10.9	4.6	61.8	22.7	0.68	0.37
NiPO-FePO (1-2)	0.33	0.3	3.5	9.5	61.7	25.1	0.52	0.41
NiPO-FePO (1-1)	0.5	0.7	2.9	10.3	60.9	25.2	0.52	0.41
NiPO-FePO (2-1)	0.66	0.2	1.9	11.6	60.7	25.6	0.53	0.42
NiPO-FePO (3-1)	0.75	0.0	1.1	11.9	61.4	25.6	0.52	0.42
NiPO-FePO (4-1)	0.8	0.0	1.3	13.5	61.4	23.9	0.62	0.39
NiPO	1.0	0.2	0.0	14.4	62.8	22.7	0.63	0.36

Table 2: Composition of the materials deposited with different FePO and NiPO ALD cycle sequences in the supercycle, metal over phosphorous (M/P) and phosphorous over oxygen (P/O) ratios are also displayed. The atomic concentrations are obtained by analysing the C 1s, Fe 3p, Ni 3p, O 1s and P 2p signals in XPS. The surface layer was removed using sputtering in the XPS-chamber before the measurement started.

P/O ratio it is clear that the materials that were deposited have quite a high P-content compared to classical phosphates. Notably, the values obtained for the M/P and P/O ratio indicate that the stoichiometry of the deposited materials deviates from the ones associated with $Ni_3(PO_4)_2$ and $FePO_4$ (M/P for $Ni_3(PO_4)_2$ and $FePO_4$ should be 1.5 and 1 resp; P/O should be .25 for both). Within the field of ALD the range of materials that are classified as phosphates is quite broad[21]. These high ratio's here obtained are in line with previous results[26] and are mainly attributed to the use of a very reactive P-precursor in TMP-plasma.

All of the as-deposited materials are amorphous as has been verified by XRD, which is in line with the original reports on the monometallic processes.

Electrocatalytic Performance of ALD-Based Metal Phosphates

To test the performance of the as-deposited metal phosphate electrocatalysts, selected samples deposited on a mirror polished Ni-disc coated with 150 nm Ni-PVD. Two series of samples have been prepared. A first one covers different compositions, comparing undoped NiPO with NiPO-FePO (1-2) and NiPO-FePO (4-1), having an Fe concentration of 3.5 at% and 1.3 at%, and an Fe to metal fraction of 27% and 9%, respectively. Two flavours of the mixed NiFePO materials have been deposited by switching the order of the NiPO and FePO ALD processes in the supercycle, implying that the surface-terminating layer is finished either with a NiPO cycle or an FePO cycle. The thickness of the deposited films was approximately 30 nm. The second series of samples comprises a thickness series for the NiPO-**FePO** (4-1) ALD process, with thicknesses ranging from 5 to 160 nm.

For electrochemical characterization, the samples were mounted on a rotating disc electrode (RDE) set-up measuring in alkaline conditions using an electrolyte of 1 M KOH. All samples underwent the same procedure, explained in detail in the Methods section. During a sequence of chronopotentiometry (CP) measurements the material is activated, followed by electrochemical impedance spectroscopy (EIS) to determine the resistance of the system for iR-compensation. Finally, cyclic voltammetry (CV) is performed, the results of which are discussed below.

Effect of Composition and Surface-Terminating Layer on Catalytic Performance

The CV-data for the first samples series is displayed in Figure 5. Graph A compare the two flavours of the NiPO-FePO (4-1) process with NiPO and the Ni-PVD coated Ni disc substrate, while graph B shows a similar comparison for the NiPO-FePO (1-2) samples. Finally graph C gives an overview of the charge transfer resistance measured for all of the samples.

Starting from the bare substrate, which shows a moderate activity, a clear improvement is already observed for the undoped NiPO layer. When Fe is introduced using the ALD supercycle approach, we notice a clear impact of the surface-terminating layer. For both the NiPO-**FePO** (4-1) and NiPO-**FePO** (1-2) samples, a significant increase in current density is observed for the films grown with the FePO process at the end of the supercycle. Both FePO terminated samples have almost identical overpotential and current density, which shows that the difference in Fe-concentration throughout the material does not yield significant differences in performance. For the NiPO-terminated layers, the **NiPO**-FePO (1-2) sample did show a higher activity than the **NiPO**-FePO (4-1), the former showing a slightly better activity compared to the undoped NiPO, while the latter performed worse than the reference. FePO terminated samples, on average, have an 18 mV lower overpotential to their NiPO terminated counterparts at 10 mA/cm^2. The fact that FePO-terminated layers clearly outperform the NiPO-terminated layers inspired an additional experiment in which the Ni-PVD coated disc was coated with 5 cycles of the FePO ALD process ($\sim$1 nm of material). For this sample a slight decrease in activity was observed compared to the bare Ni-PVD Figure S7 in Supporting Materials, highlighting that a NiPO-based matrix is necessary.

Figure 6 shows that the difference in ALD sequence also resulted in different redox peaks. For NiPO and the **NiPO**-FePO (4-1) material, the two peaks in the forward scan appear at the same positions (1.38 V and 1.41 V, resp.), while for the FePO-terminated NiPO-**FePO** (4-1) material a peak appears at more positive potential (1.43 V). For the NiPO-FePO (1-2) samples, a broad bump is observed at 1.41 V for the NiPO-terminated sample, which is again shifted to higher potentials for the FePO-terminated sample. In addition, a peak at 1.45 V is present for both flavors. Identifying the exact nature of the (multiple convoluted) oxidation and reduction peaks is complex for the amorphous Fe-doped Ni phosphate materials, and is considered out of the scope here. For FeNiO catalysts, the main oxidation peak is attributed to the $Ni(OH)_2$ to NiOOH transition, and with more Fe incorporated a shift to more positive anodic potentials was reported [11]. Here, we obtain a similar shift by only changing the surface-terminating layer from NiPO to FePO in the ALD process, especially for the NiPO-FePO (4-1) materials.

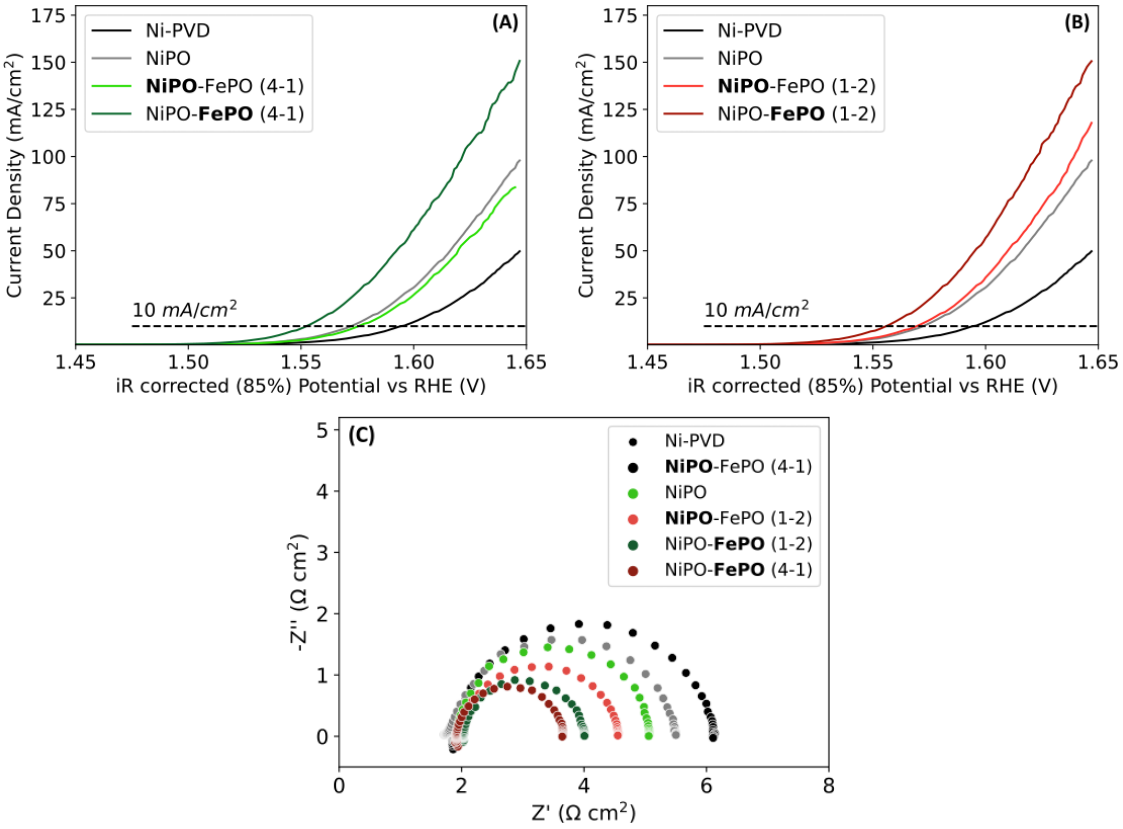

Figure 5: Selected cyclic voltammograms for activated ALD thin films with different compositions. The CV-data is 85% iR-corrected and the displayed data is always the 5th forward sweep of the CV performed at 1 mV/s and 900 rpm. Bold font indicates the surface terminating layer. (A) Comparison between bare Ni-PVD, NiPO and NiPO-FePO (4-1) materials. (B) Comparison between bare Ni-PVD, NiPO and NiPO-FePO (1-2) materials. (C) EIS measurements taken at an applied voltage of 0.626 V vs HgO/Hg (1.572 V vs RHE) indicate that the charge transfer resistance decreases in line with the better performing ALD layer.

Effect of Film Thickness on Catalytic Performance

The effect of increasing the number of ALD supercycles and thus the overall thickness of the catalyst film is shown in Figure 7. The films were deposited using the NiPO-**FePO** (4-1) ALD process, i.e. with FePO as the surface-terminating layer. An overall increasing trend is observed, with thicker films resulting in a higher current density. The overall decrease in overpotential at 10 mA/cm^2 is 60 mV when comparing the 160 nm layer with the uncoated disc. Likewise, the integrated area of the pre-OER redox waves, as a measure for the number of metal ions participating in the oxidation and reduction reactions, increases with increasing film thickness, as inferred from Figure 8 (A). The positive correlation between the oxidation peak current density and the film thickness (Figure 8 (B)) also indicates an increase in the amount of electrochemically active substance with increasing catalyst volume.

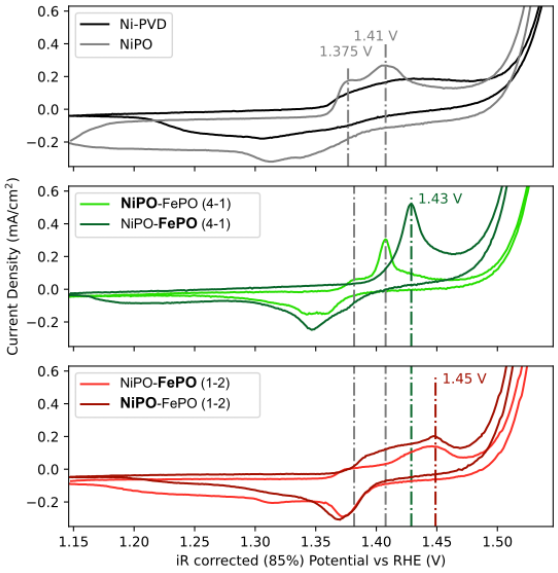

Figure 6: Zoom-in of the cyclic voltammograms of figure 5 in the pre-OER potential region. The notation in bold indicates the surface terminating layer.

Discussion

From the electrochemical characterization of the two series of samples prepared for this work, it can be concluded that both the surface and the volume of the ALD NiPO-FePO films impact the OER activity. The current density is significantly higher if FePO is the surface-terminating layer in the ALD process (Figure 5), while thicker films also result in an improved OER activity (Figure 7).

To interpret the impact of a change in cycle sequence in the ALD supercycle, it is instructive to reason about the distribution of the metal atoms in the NiPO-FePO deposited materials. While supercycle ALD often results in homogeneously mixed materials, in certain occasions layered structures with graded interfaces may form [29]. This is the case when the diffusion length of a metal species in the adjacent layer (e.g. Fe in NiPO and/or Ni in FePO) is smaller than the thickness of that adjacent layer. Importantly, in the case of the NiPO-FePO ALD process used in this work, the average GPC of 0.32 nm/cycle for the mixed process is large compared to typical values for oxide ALD processes, related to the use of TMP*. This implies a NiPO layer thickness of 1.28 nm for the NiPO-FePO (4-1) process.
Previous work showed intermixing of Ti and Al in TiAlO ALD layers up to 0.38 nm individual layer thickness, while for thicker TiO_2 or Al_2O_3 layers a nanolaminate structure was found [36]. In another study, HfO_2 and Al_2O_3 were shown to intermix on a scale of 0.5 nm [37]. Therefore, it can be reasonably assumed that the Fe atoms are not homogeneously distributed within the relatively thick adjacent NiPO layers but that intermixed regions and NiPO regions alternate (Figure 9). While the concentration and distribution of Ni and Fe atoms within the bulk of the thin film will not be impacted by the order of the ALD processes in the supercycle sequence, the composition of the very surface layer and in particular the surface concentration of Fe centers will largely depend on this order. The processes ending with FePO ALD are likely to generate a surface with mixed composition. From Figure 5, it can be concluded that this is beneficial for the OER. Along the same lines, the higher activity of the **NiPO**-FePO (1-2) sample compared to the **NiPO**-FePO (4-1) can possibly be explained by the lower thickness of the NiPO capping layer in the **NiPO**-FePO (1-2) sample, exposing more FePO at the surface.

A change in the surface termination of thin layers that otherwise have similar internal composition and structure also affects the redox signature (Figure 6), with a shift of the oxidation peak to higher potentials for an FePO surface-terminating layer in the ALD process. For all metal phosphate samples plotted in Figure 6, the film thickness was the same (30 $\pm$ 3 nm), and hence effects of the film resistance and electrochemical active surface area on the line shape of the oxidation peak should be comparable. The CV-scans also seem to indicate this, only the pure NiPO sample has a

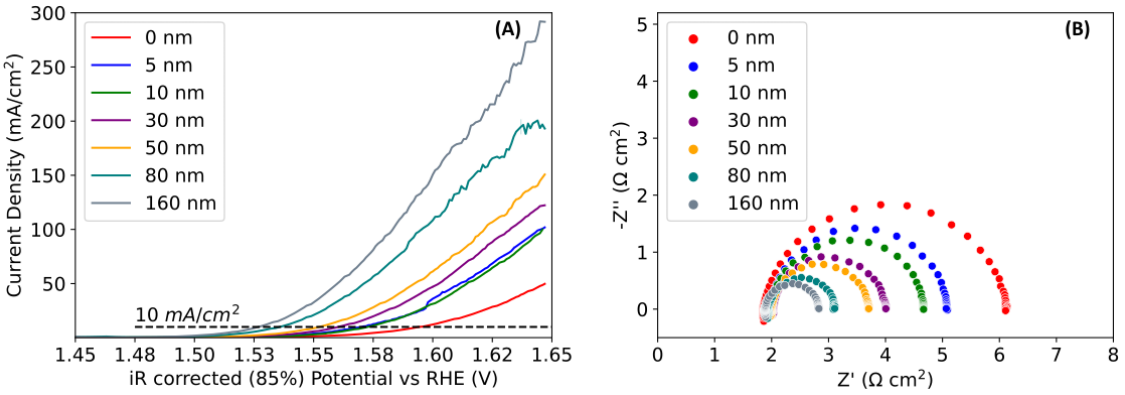

Figure 7: (A) Selected cyclic voltammograms for activated NiPO-**FePO** (4-1) thin films with different thicknesses. The CV-data is 85% iR-corrected and the displayed data is always the 5th forward sweep of the CV performed at 1 mV/s and 900 rpm. (B) EIS measurements indicating a decrease in charge transfer resistance as the thickness of the material increases.

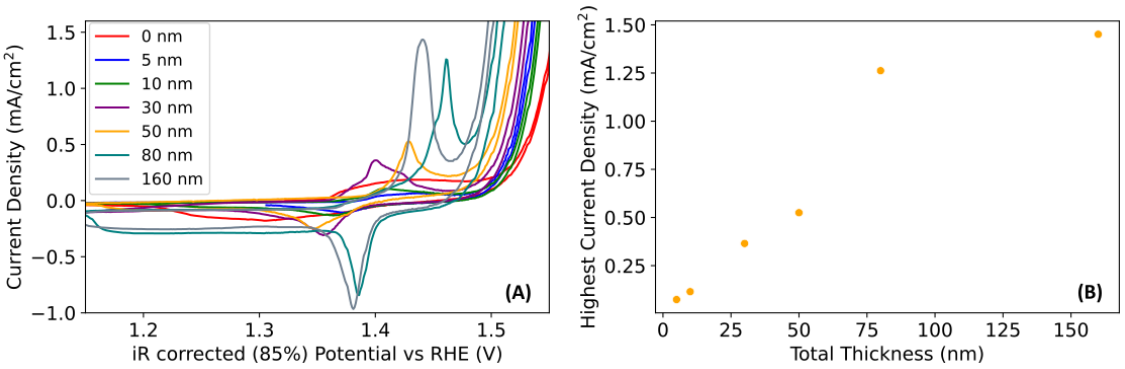

Figure 8: (A) Zoom-in of the cyclic voltammograms of figure 7 in the pre-OER potential region. (B) Oxidation peak current density as a function of the catalyst film thickness.

higher capacitive current, indicating a higher surface area. Therefore, it is reasonable to directly link the peak shift with a difference in the nature of the active species formed during catalyst activation and operation, with more active centers for OER created when the ALD process is terminated with an FePO cycle.

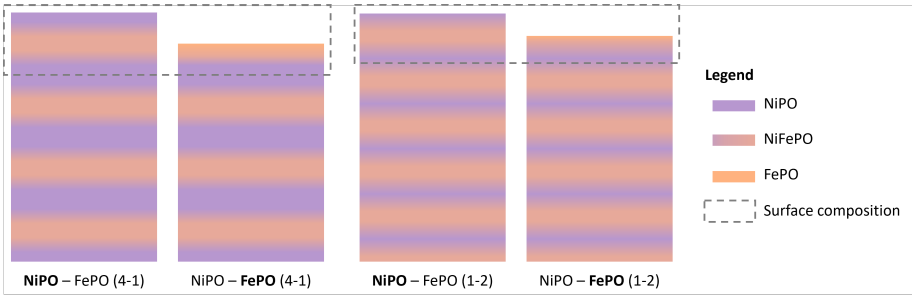

Figure 9: Artists impression of the expected structure of the deposited ALD materials. Both NiPO - FePO (4-1) and NiPO - FePO (1-2) are rich in Ni (90% and 70% respectively). Bold font indicates the surface terminating layer used in the ALD sequence.

The increase in OER current and electrochemical active surface area (ECSA) with film thickness (Figure 7 and 8) resembles the results established by Klingan et al. [38] for electrodeposited thin films of the so-called Co-Pi or CoCat catalyst, an amorphous cobalt-based hydroxide that also contains phosphate ions [39]. They concluded that OER catalysis takes place throughout the volume of the amorphous and hydrated oxide material. Another recent publication by Zhang et al.[22] discovered that ALD-deposited CoPi-layers restructure over time while being cycled in a basic electrolyte. This restructuring resulted in the conversion of a more phosphorous rich material to an oxide or hydroxide material losing a sizeable fraction of its P-content. Over the course of the cycling the ECSA of the material significantly increased by a factor of 40. Hence, our results suggest the conversion of the as-deposited smooth and continuous ALD films into ion-permeable structures during catalyst activation and operation, potentially promoted by the presence of phosphorous in the films.

In addition to an increase in oxidation peak current with film thickness, Figure 8 also shows a change in peak line shape and potential. However, in this case, other aspects than the nature of the active centers can influence the relative peak positions, such as variations in film resistance and capacitive current due to the differences in thickness and active surface area. Notably, for the electrodes with 80 and 160 nm catalyst layers, an increase in capacitance can be seen in Figure 8 (A), as evidenced by the difference in capacitive current between the forward and backward scan below 1.3 V (vs. RHE).

In summary, firstly, the chemical composition of the top few atomic layers of the NiFePO materials has a decisive impact on the OER current densities and the nature of the active center. Secondly, OER catalysis is not restricted to the outer surface of the NiFePO thin film catalysts; increasing the film thickness and hence catalyst volume results in higher current densities and a larger ECSA. The significant role of the surface termination for a volume-active catalyst is remarkable. We conservatively conclude that the surface termination impacts the restructuring process of the thin film catalyst, not exclusively at its outer surface but also within its volume.

Conclusion

This work investigates for the first time a bimetallic phosphate grown by ALD as (pre)catalyst for the oxygen evolution reaction in an alkaline medium at room temperature. Iron-doped nickel phosphates have been obtained via an ALD supercycle approach, based on alternating PE-ALD cycles of nickel phosphate and iron phosphate. Analysis of the average growth per cycle (GPC) and the composition of the bimetallic phosphates indicates strong deviations from the rule of mixtures. The average GPC of 0.32 nm/cycle is almost twice as high as the expected value. Moreover, Ni and Fe do not get incorporated in the film in the expected ratios. The deposition of Ni phosphate is greatly enhanced in a mixed process with Fe phosphate compared to the pure Ni phosphate process. Additional experiments have ruled out that significant differences in surface roughness or decomposition of the Ni precursor on an iron phosphate would lie at the origin of these observations. We hypothesize that the presence of the iron phosphate creates reactive species favorable for the nickel phosphate to be incorporated into the film, but the exact nature of these remains to be elucidated.

The developed supercycle ALD approach allows to deposit iron-doped nickel phosphate OER catalysts with excellent control over the internal composition as well as the composition of the surface-terminating layer. For example, an iron-doped nickel phosphates with an Fe to metal fraction of 9% can be achieved by alternating 1 iron phosphate and 4 nickel phosphate ALD cycles. By switching the order of the nickel phosphate and iron phosphate ALD processes in the supercycle, two flavours of this material have been obtained. While this variation in ALD is usually considered to have minimal impact on the thin film properties of mixed films, we find a striking impact on the OER activity, which we relate to a difference in surface composition. The flavour obtained with the process ending with iron phosphate ALD results in a 20 mV reduction of the overpotential at 10 mA/cm^2 and 50% larger current densities at 1.65 V compared to the nickel phosphate-terminated flavour. We relate this result to limited intermixing of Fe and Ni via the supercycle approach. Therefore, the process ending with iron phosphate ALD will achieve a higher concentration of iron centers on the surface of the otherwise equal mixed phosphate thin film, highlighting the importance of the surface chemistry on the catalyst activation and operation.

Similar results and OER performances have been obtained for an iron-doped nickel phosphate with an Fe to metal fraction of 27%, suggesting that the difference in Fe-concentration throughout the material does not yield significant differences. Increasing the film thickness, on the other hand, has a significant impact on the OER current density and the number of metal ions participating in the non-catalytic oxidation and reduction reactions, and both are found to increase with increasing film thickness. This result is in line with previous reports for an amorphous Co oxide catalyst with phosphate ions, and suggests that also the volume of the thin film is catalytically active.

It can be concluded that both the surface and the volume of the ALD-grown iron-doped nickel phosphates determine the OER activity. By leveraging the ALD supercycle approach to synthesize thin films with the same distribution of atoms in the bulk but different surface composition, our results show that the surface species are most critical in the catalyst restructuring process and formation of the actual OER catalytic centers, even if the amorphous phosphate materials are volume-active.

Our results indicate that the ability of ALD to tune the surface and bulk composition of electrocatalyst thin films can be highly beneficial to investigate relationships between the precatalyst surface and activity for amorphous materials. Future work should focus on unraveling the details of the surface chemistry and restructuring process.

Acknowledgements

References

1. IEA. *Global Hydrogen Review 2023* `https://www.iea.org/reports/global-hydrogen-review-2023` (2023).
2. Karakaya, E. *et al.* Potential transitions in the iron and steel industry in Sweden: Towards a hydrogen-based future? *Journal of Cleaner Production* **195,** 651–663. ISSN: 0959-6526 (2018).
3. Man, I. C. *et al.* Universality in Oxygen Evolution Electrocatalysis on Oxide Surfaces. *ChemCatChem* **3,** 1159–1165 (2011).
4. Giordano, L. *et al.* pH dependence of OER activity of oxides: Current and future perspectives. *Catalysis Today* **262.** Electrocatalysis, 2–10. ISSN: 0920-5861 (2016).
5. Liu, Z. *et al.* The effect of membrane on an alkaline water electrolyzer. *International Journal of Hydrogen Energy* **42,** 29661–29665. ISSN: 0360-3199 (2017).
6. Zhang, K. *et al.* Advanced Transition Metal-Based OER Electrocatalysts: Current Status, Opportunities, and Challenges. *Small* **17,** 2100129 (2021).
7. Jamesh, M.-I. *et al.* Tuning the electronic structure of the earth-abundant electrocatalysts for oxygen evolution reaction (OER) to achieve efficient alkaline water splitting – A review. *Journal of Energy Chemistry* **56,** 299–342. ISSN: 2095-4956 (2021).
8. Trotochaud, L. *et al.* Nickel–Iron Oxyhydroxide Oxygen-Evolution Electrocatalysts: The Role of Intentional and Incidental Iron Incorporation. *Journal of the American Chemical Society* **136.** PMID: 24779732, 6744–6753 (2014).
9. Landon, J. *et al.* Spectroscopic Characterization of Mixed Fe–Ni Oxide Electrocatalysts for the Oxygen Evolution Reaction in Alkaline Electrolytes. *ACS Catalysis* **2,** 1793–1801 (2012).
10. Trotochaud, L. *et al.* Solution-Cast Metal Oxide Thin Film Electrocatalysts for Oxygen Evolution. *Journal of the American Chemical Society* **134.** PMID: 22991896, 17253–17261 (2012).
11. Louie, M. W. *et al.* An Investigation of Thin-Film Ni–Fe Oxide Catalysts for the Electrochemical Evolution of Oxygen. *Journal of the American Chemical Society* **135.** PMID: 23859025, 12329–12337 (2013).
12. Li, Y. *et al.* Iron-Doped Nickel Phosphate as Synergistic Electrocatalyst for Water Oxidation. *Chemistry of Materials* **28,** 5659–5666 (2016).
13. Liu, M. *et al.* Cover Feature: Cobalt-Iron Pyrophosphate Porous Nanosheets as Highly Active Electrocatalysts for the Oxygen Evolution Reaction (ChemElectroChem 1/2018). *ChemElectroChem* **5,** 3–3 (2018).
14. Shao, Y. *et al.* Single-Crystal Cobalt Phosphate Nanosheets for Biomimetic Oxygen Evolution in Neutral Electrolytes. *Angewandte Chemie International Edition* **58,** 14599–14604 (2019).
15. Di Palma, V. *et al.* Atomic layer deposition of cobalt phosphate thin films for the oxygen evolution reaction. *Electrochemistry Communications* **98,** 73–77. ISSN: 1388-2481 (2019).
16. Mohanty, R. I. *et al.* Iron Cobalt Phosphonate Derived Heteroatom Doped Metal Oxides as Superior Electrocatalysts for Water Oxidation Reaction. *ChemCatChem* **15,** e202300731 (2023).
17. Guo, R. *et al.* Phosphate-Based Electrocatalysts for Water Splitting: Recent Progress. *ChemElectroChem* **5,** 3822–3834 (2018).
18. Lin, L. *et al.* Rapid fabrication of FexNi2-xP4O12 and graphene hybrids as electrocatalyst for highly efficient oxygen evolution reaction. *Applied Catalysis B: Environmental,* 122834. ISSN: 0926-3373 (2023).
19. Chen, J. *et al.* Recent Advances in the Understanding of the Surface Reconstruction of Oxygen Evolution Electrocatalysts and Materials Development. *Electrochemical Energy Reviews* **4,** 566–600 (2021).
20. Li, R. *et al.* Insights into Correlation among Surface-Structure-Activity of Cobalt-Derived Pre-Catalyst for Oxygen Evolution Reaction. *Advanced Science* **7,** 1902830 (2020).
21. Henderick, L. *et al.* Atomic layer deposition of metal phosphates. *Applied Physics Reviews* **9,** 011310 (2022).
22. Zhang, R. *et al.* Electrochemical Activation of Atomic Layer-Deposited Cobalt Phosphate Electrocatalysts for Water Oxidation. *ACS Catalysis* **11.** PMID: 33842021, 2774–2785 (2021).
23. Rongé, J. *et al.* Bifunctional earth-abundant phosphate/phosphide catalysts prepared via atomic layer deposition for electrocatalytic water splitting. *Nanoscale Adv.* **1,** 4166–4172 (10 2019).

24. Kawashima, K. *et al.* Accurate Potentials of Hg/HgO Electrodes: Practical Parameters for Reporting Alkaline Water Electrolysis Overpotentials. *ACS Catalysis* **13,** 1893–1898 (2023).
25. Anantharaj, S. *et al.* How properly are we interpreting the Tafel lines in energy conversion electrocatalysis? *Materials Today Energy* **29,** 101123. ISSN: 2468-6069 (2022).
26. Dobbelaere, T. *et al.* Plasma-Enhanced Atomic Layer Deposition of Iron Phosphate as a Positive Electrode for 3D Lithium-Ion Microbatteries. *Chemistry of Materials* **28,** 3435–3445 (2016).
27. Henderick, L. *et al.* Plasma-enhanced atomic layer deposition of nickel and cobalt phosphate for lithium ion batteries. *Dalton Trans.* **51,** 2059–2067 (5 2022).
28. Dobbelaere, T. *et al.* Atomic Layer Deposition of Aluminum Phosphate Based on the Plasma Polymerization of Trimethyl Phosphate. *Chemistry of Materials* **26,** 6863–6871 (2014).
29. Mackus, A. J. M. *et al.* Synthesis of Doped, Ternary, and Quaternary Materials by Atomic Layer Deposition: A Review. *Chemistry of Materials* **31,** 1142–1183 (2019).
30. Monaco, L. *et al.* XPS study on the passivity of coarse-grained polycrystalline and electrodeposited nanocrystalline nickel-iron (NiFe) alloys. *Corrosion Science* **176,** 108902. ISSN: 0010-938X (2020).
31. Chong, Y. T. *et al.* Direct Atomic Layer Deposition of Ternary Ferrites with Various Magnetic Properties. *Chemistry of Materials* **22,** 6506–6508 (2010).
32. Espejo, A. P. *et al.* Magnetic and electrical characterization of nickel-rich NiFe thin films synthesized by atomic layer deposition and subsequent thermal reduction. *Nanotechnology* **27,** 345707 (2016).
33. Baker, J. G. *et al.* Nucleation Effects in the Atomic Layer Deposition of Nickel–Aluminum Oxide Thin Films. *Chemistry of Materials* **32,** 1925–1936 (2020).
34. Schneider, J. R. *et al.* Understanding and Utilizing Reactive Oxygen Reservoirs in Atomic Layer Deposition of Metal Oxides with Ozone. *Chemistry of Materials* **34,** 5584–5597 (2022).
35. Schneider, J. R. *et al.* The Influence of Ozone: Superstoichiometric Oxygen in Atomic Layer Deposition of Fe2O3 Using tert-Butylferrocene and O3. *Advanced Materials Interfaces* **7,** 2000318 (2020).
36. Sintonen, S. *et al.* X-ray reflectivity characterization of atomic layer deposition Al2O3/TiO2 nanolaminates with ultrathin bilayers. *J. Vac. Sci. Technol. A* **32,** 01A111 (2013).
37. Ho, M.-Y. *et al.* Suppressed crystallization of Hf-based gate dielectrics by controlled addition of Al2O3 using atomic layer deposition. *Applied Physics Letters* **81,** 4218–4220 (2002).
38. Klingan, K. *et al.* Water Oxidation by Amorphous Cobalt-Based Oxides: Volume Activity and Proton Transfer to Electrolyte Bases. *ChemSusChem* **7,** 1301–1310 (2014).
39. Kanan, M. W. *et al.* In Situ Formation of an Oxygen-Evolving Catalyst in Neutral Water Containing Phosphate and Co¡sup¿2+¡/sup¿. *Science* **321,** 1072–1075 (2008).